Electro-osmotic flows through topographically complicated porous media: Role of electropermeability tensor

Aditya Bandopadhyay,[1] Debabrata DasGupta,[2] Sushanta K. Mitra,[3] and Suman Chakraborty[1,2,*]
[1]*Advanced Technology Development Center, Indian Institute of Technology Kharagpur, Kharagpur, India, 721302*
[2]*Department of Mechanical Engineering, Indian Institute of Technology Kharagpur, Kharagpur, India, 721302*
[3]*Micro and Nano-scale Transport Laboratory, University of Alberta, Canada, T6G 2G8*
(Received 26 September 2012; revised manuscript received 15 January 2013; published 12 March 2013)

In the present work, we consider a framework for characterizing electro-osmotic flows in topographically complicated porous media and derive an effective up-scaled transport parameter to quantify this. We term this parameter the electro-permeability, which characterizes the electro-osmotic flow through composite porous media in analogy with Darcy's law. The electro-permeability tensor, thus introduced, serves a simple means of relating the volume flow rate with the applied electric field without going into the intricacies of the microstructure of the porous domain. First, we consider cases where the solid fractions have a fractal dimension generated by the Mandelbrot set, purely for the sake of demonstration. Based on such considerations, we employ the method of homogenization to obtain the effective electro-permeability parameter from the numerical simulations executed over a representative volume element. Our derived electro-permeability tensor components exhibit functional relationships with the solid or liquid fraction as well as the topography of the porous medium. Having established these functional relationships, we evaluate the tensor components for a binary composite porous medium in which one constituent has markedly high ζ potential than the other constituent, for illustration with potential relevance in microfluidics. We establish the sensitivity of the electro-permeability tensor on the domain morphology, solid fraction, ratio of solid fractions of the two phases having the two different ζ potential values, and the ζ potential contrast and compare it with equivalent Darcy permeability for the same. We thus provide a simple mathematical framework that may be immensely helpful for devising a computationally efficient way of characterizing electro-osmosis through topographically complicated porous media.

DOI: 10.1103/PhysRevE.87.033006 PACS number(s): 47.61.−k

I. INTRODUCTION

With increasing applications of flows through membranes (e.g., proton exchange membranes [1]), nanoporous media (for energy conversion [2–4]), and fibrous media (e.g., paper microfluidics [5,6]), it is imperative to address the transport of colloids and aqueous solutions through a domain that is characterized by a tortuous and highly networked path [7]. In the traditional paradigm of pressure-driven flows through porous media, one typically refers to Darcy's law in addressing such scenarios, which relates the volume flow rate to the applied pressure gradient via the permeability parameter [8]. An inherent simplicity of Darcy's law stems from the fact that it may accommodate various correlations in order to represent the consequences of inherent topographical features like porosity and tortuosity in the flow analysis. However, despite its inherent simplicity, use of it is often restricted by its obvious limitations in explicitly capturing the consequences of complicated topography of the domain from a rather fundamental perspective. The situation gets even more challenging when electro-osmosis occurs within the flow domain, by virtue of an intricate interaction between a charged interfacial layer formed at the solid-liquid interface, also known as the electrical double layer (EDL), and an externally applied electric field [9–22]. Implications of the topography of the porous medium on the resultant flow characteristics, under such circumstances, may remain far from being trivial, because of combined multiphysics and multiscale nature of the underlying transport processes.

In an analogy to Darcy's law, here we develop an effective electro-permeability parameter which would relate the volume flow rate with the applied electric field for electro-osmotic flow in porous media. Electro-osmosis through porous media has found applications in areas like: soil dewatering, enhanced oil recovery in bitumen [23], proton exchange membranes in fuel cells [1,24,25], flows involving suspensions of charged particles [26,27], and liquid transfers in soils [25]. As such, electro-osmotic transport in a porous medium is a complicated interplay of the EDL [23,29], the topographical feature of the flow domain, and the applied electric field, which may best be addressed in a computationally efficient manner by employing the concepts of multiple physical scales.

A wide variety of physical problems have multiple scales integrated into the physics of the problem. A few such problems are flows in porous media, turbulent flows, analysis of composite materials, and many more [30–36]. Usually these problems involve complex geometries or topographies and hence are quite often not analytically tractable. For example, flows of Newtonian fluids in porous media involve the solution of the full Navier-Stokes equation in a complex domain. The situation may be further complicated by the fact that in order to capture the underlying physics of the problem (for instance, flows through tortuous channels bearing surface potential), we are required to resolve the computational domain to the smallest length scale so that the local fluctuations are captured. Failure to resolve the domain to the smallest domain of interest may lead to physically unrealistic solutions because of the inability to capture the physics which has its genesis in the

*suman@mech.iitkgp.ernet.in

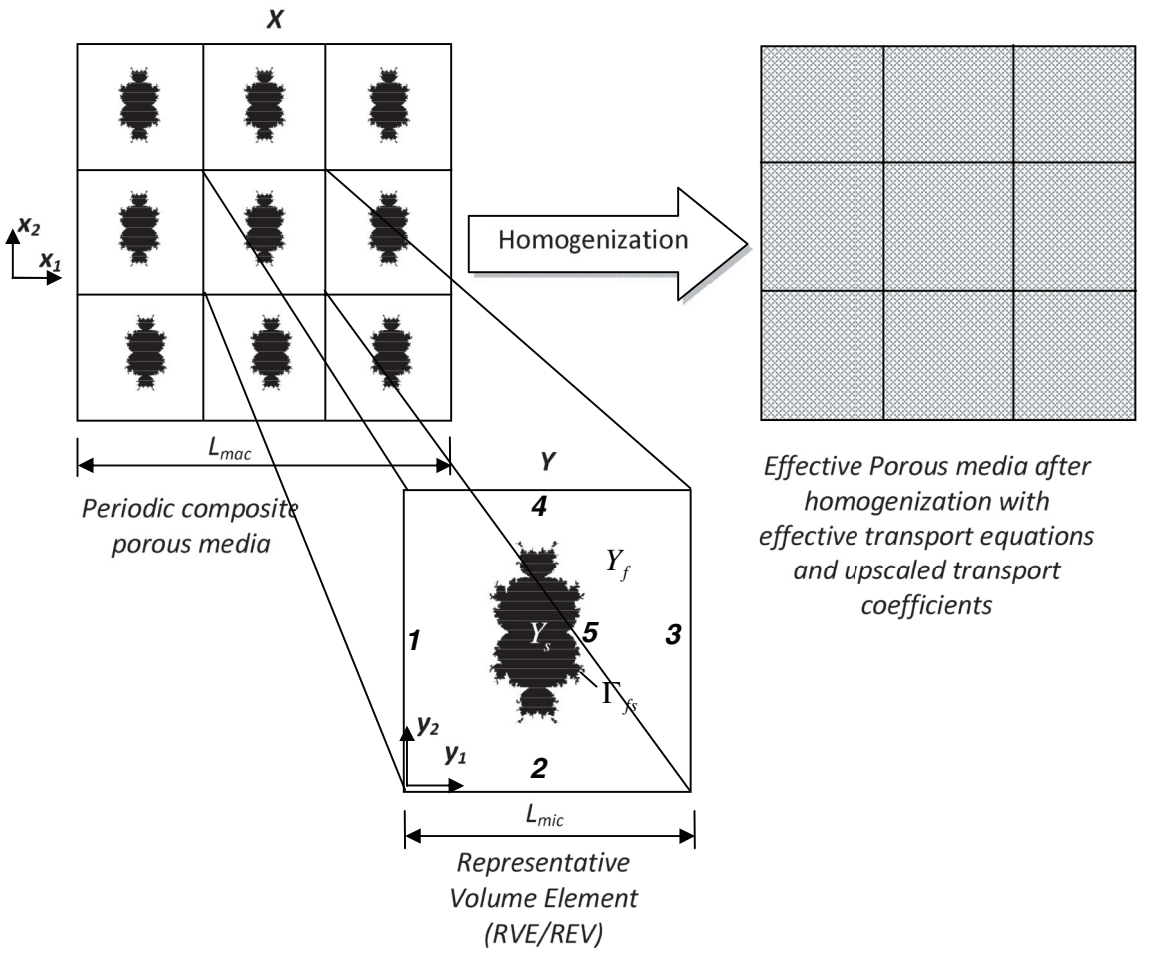

FIG. 1. Schematic of the spatially periodic cells. Boundary pairs (1, 3) and (2, 4) in the Representative volume element (RVE or REV) are periodic, whereas boundary 5 is the interior boundary, which represents the boundary of the solid microstructure.

smallest possible physical scale. However, as a computationally inexpensive alternative to the full-scale simulation process, one may exploit a mathematical up-scaling procedure inside a small portion of the domain (a representative volume element) by the virtue of which it is possible to absorb the combined effect of the topography and field variables in terms of a generalized up-scaled constitutive functional relationship.

In an effort to implement the above conceptual paradigm for analyzing electro-osmotic transport [9,11–13,15,16,23,36–39] through porous media, we employ the method of homogenization [33,35,40–42]. The method of homogenization is a powerful tool for obtaining effective equations and computing effective parameters in problems where phenomena occur at various well-separated length and time scales. Thus, under an assumption of scale separation, it enables one to analyze the effects of fluctuations of field variables over different length scales in a coupled manner. This is achieved by obtaining mathematically homogenized (or effective) properties over a macroscopic control volume, based on variation of field variables over many microscopic cells that constitute the volume element. Since the effective property carries information of transport features over microscopic length scales, it is expected to represent the microscale physics in a macromodel in a much more rigorous and efficient manner than what a simple volume averaging does.

In the present work, we first apply the method of homogenization for analyzing electro-osmotic transport through porous medium. As a consequence, we establish a functional relationship between an effective electro-permeability parameter and the solid fraction in the domain as well as a chosen topographical parameter. We then apply this model to evaluate the electro-permeability tensor components for a binary composite porous medium in which one constituent has markedly high ζ potential than the other constituent, as a demonstrative example.

II. MATHEMATICAL MODELING

We consider a periodically repeating volume element in the flow domain as shown in the schematic shown in Fig. 1. The main assumption concerning this spatial periodicity is that the cells $\boldsymbol{Y}$ repeat themselves at well-separated length scales to form the heterogeneous media $\boldsymbol{X}$. Such a periodic block is referred as the representative volume element (known as RVE or analogously REV, representative elemental volume; highlighted in Fig. 1), which contains all the small details of the microstructure [43,44]. The unit cell $\boldsymbol{Y}$ is formed by two parts Y_s and Y_f representing the solid and liquid parts of the domain, respectively. The boundaries 1, 2, 3, and 4 constitute the boundaries of the RVE such that boundary pairs (1, 3) and

(2, 4) are periodic and boundary 5, represented as Γ_{fs}, is the interface separating Y_s and Y_f.

Before introducing a formal implementation of the method of homogenization as applied to the porous media in the context of electro-osmotic transport, we first mention the governing equations for electrical potential distribution because of the presence of surface charges on the walls of the porous media, which is central to the phenomenon of electro-osmosis.

A. EDL potential distribution induced in the porous medium

The potential distribution (ψ) in the EDL is coupled with the charge density distribution (ρ_e) through the Poisson equation, as given by [29]

$$\nabla^2\psi = -\rho_e/\varepsilon_r, \tag{1}$$

where

$$\rho_e = e(z^+n^+ + z^-n^-). \tag{2}$$

Here ε_r is the permittivity of the media, e is the protonic charge, z^+ and z^- represent the valency of positive and negatively charged species respectively, and n^+ and n^- represent the ionic number densities of the positive and negative species, respectively. The ionic number densities are assumed to be described by the Boltzmann distribution [29], which is given as

$$n_\pm = n_0 \exp(-z^\pm e\psi/k_BT), \tag{3}$$

where n_0 is the bulk ionic concentration, k_B is the Boltzmann constant, and T is the absolute temperature. For a z: z symmetric electrolyte, Eqs. (1)–(3) can be combined together to yield the Poisson-Boltzmann equation [29]:

$$\nabla^2\psi = \frac{2zen_0}{\varepsilon_r}\sinh\left(\frac{ze\psi}{k_BT}\right). \tag{4}$$

Equation (4) is subjected to ζ potential at the shear plane (effectively the interface between the wall-adhering immobile ionic layer and the outer mobile ionic layer; here applied at boundary 5 in Fig. 1) and periodic boundary conditions on the RVE/REV boundaries.

B. Hydrodynamic equations

The corresponding governing transport equations for a steady flow of Newtonian fluid are

$$\vec{\nabla}\cdot\vec{v} = 0, \tag{5}$$

$$\rho\vec{v}\cdot\vec{\nabla}\vec{v} = -\vec{\nabla}p + \mu\nabla^2\vec{v} + \rho_e\vec{E}. \tag{6}$$

Equation (5) represents the continuity equation, and Eq. (6) represents the momentum equation with an augmented body force term, which is derived from the Maxwell stress tensor [10]. Here $\vec{v}$ is the flow velocity, p is the pressure, μ is the viscosity, and $\vec{E}$ is the electrical field. Equation (6) is subject to no slip and no flux at the solid boundaries bounding the topographically complex domain present in each RVE/REV (boundary 5 in Fig. 1) and periodicity on the RVE/REV boundaries.

C. Applied potential field

In addition to the EDL potential field, an electric field due to the externally applied voltage is also established. The later satisfies the Laplace equation [29,45] as given by

$$\nabla^2\phi = 0. \tag{7}$$

Equation (7) is subject to no electric flux on the solid boundaries bounding the topographically complex domain present in each RVE/REV (boundary 5 in Fig. 1), and Dirichlet boundary conditions on two parallel boundaries (for example, boundaries 1 and 3 for an electric field applied along the x_1 direction), and periodic on the other two of the RVE/REV boundaries (for example, boundaries 2 and 4 for an electric field applied along the x_1 direction).

D. Asymptotic expansion and homogenized equations

We nondimensionalize the governing equations and boundary conditions with the following parameters: $\bar{x}_i = x_i/L_{\text{mac}}$, $\bar{y}_i = y_i/L_{\text{mic}}$, $\bar{\psi} = \psi/\zeta$, $\bar{\phi} = \phi/\phi_{\text{ref}}$, $\bar{v}_i = v_i/U_{\text{ref}}$, $E_{\text{ref}} = \phi_{\text{ref}}/L_{\text{mac}}$, and $\bar{\nabla}\bar{p} = \nabla p/(\nabla p)_{\text{ref}}$ where $U_{\text{ref}} = (\varepsilon_r\zeta\phi_{\text{ref}})/(L_{\text{mac}}\mu)$, $(\nabla p)_{\text{ref}} = \mu U_{\text{ref}}/L^2_{\text{mac}}$ where L_{mac} and L_{mic} are the characteristic length scale of the macroscopic and microscopic domains respectively, ε_r is the permittivity of the medium, and ζ is the wall ζ potential.

If the number of microscopic periodically repeating unit cells constituting the macroscopic domain is small, the ratio of the characteristic micro to the macrolength scale, $(L_{\text{mic}}/L_{\text{mac}})$, is not small, and the assumption of the separation of scale fails. In such cases, the effective property is not an intrinsic one, and there is no effective description of the porous medium. Therefore, the fundamental requirement is that the scales must be separated such that the condition $\varepsilon = L_{\text{mic}}/L_{\text{mac}} \ll 1$ is satisfied. If the separation of scales is valid, any field quantity may effectively be represented as a function of these two separated variables $\bar{x}$ and $\bar{y}$. Under the premise of scale separation, we next proceed to expand different variables asymptotically in terms of the small parameter ε [36,42–44]. The asymptotic expansions of the physical fields are given as

$$\bar{v}^\varepsilon = \bar{v}_i^0(\bar{\bar{x}},\bar{\bar{y}}) + \varepsilon\bar{v}_i^1(\bar{\bar{x}},\bar{\bar{y}}) + \varepsilon^2\bar{v}_i^2(\bar{\bar{x}},\bar{\bar{y}}) + O(\varepsilon^3), \tag{8a}$$

$$\bar{p}^\varepsilon = \varepsilon^s\bar{p}_0(\bar{\bar{x}},\bar{\bar{y}}) + \varepsilon^{s+1}\bar{p}_1(\bar{\bar{x}},\bar{\bar{y}}) + \varepsilon^{s+2}\bar{p}_2(\bar{\bar{x}},\bar{\bar{y}}) + O(\varepsilon^{s+3}), \tag{8b}$$

$$\bar{\psi}^\varepsilon(\bar{\bar{x}},\bar{\bar{y}}) = \varepsilon^e\bar{\psi}_0(\bar{\bar{x}},\bar{\bar{y}}) + \varepsilon^{e+1}\bar{\psi}_1(\bar{\bar{x}},\bar{\bar{y}}) + \varepsilon^{e+2}\bar{\psi}_2(\bar{\bar{x}},\bar{\bar{y}}) + O(\varepsilon^{e+3}), \tag{8c}$$

$$\bar{\phi}^\varepsilon = \varepsilon^q\bar{\phi}_0(\bar{\bar{x}},\bar{\bar{y}}) + \varepsilon^{q+1}\bar{\phi}_1(\bar{\bar{x}},\bar{\bar{y}}) + \varepsilon^{q+2}\bar{\phi}_2(\bar{\bar{x}},\bar{\bar{y}}) + O(\varepsilon^{q+3}), \tag{8d}$$

The thermo-physical properties in a multiscale approach are given as

$$\mu^\varepsilon = \varepsilon^a\mu_0, \tag{9a}$$

$$\rho^\varepsilon = \varepsilon^b\rho_0, \tag{9b}$$

and

$$\varepsilon_r^\varepsilon = \varepsilon^c\varepsilon_{r,0}. \tag{9c}$$

The values of the parameters s, e, q, a, b, and c can be determined by equating the different terms of the governing transport equations depending on their relative importance. The expansion terms given above are then introduced into the governing transport equations with the definition of the total differential operator as [43,44] $\frac{D}{D\bar{x}_i} \sim \bar{\nabla}_x + \varepsilon^{-1}\bar{\nabla}_y$ where $\bar{\nabla}_x$ and $\bar{\nabla}_y$ represent the gradient operators with respect to $\bar{x}$ and $\bar{y}$ respectively. We obtain the following set of non-dimensional equations, which describe the electro-osmotic flow through a representative volume element and will be used subsequently for homogenization. While nondimensionalizing the transport equations, we multiply the terms with the orders of the respective dimensionless groups:

$$\bar{\nabla}\cdot\bar{\vec{v}} = 0, \tag{10}$$

$$\varepsilon^{b-a}\mathrm{Re}\vec{v}\cdot\bar{\nabla}\bar{\vec{v}} = -\varepsilon^{-a}\bar{\nabla}\bar{p} + \bar{\nabla}^2\bar{\vec{v}} + \varepsilon^{c-a}\bar{\nabla}^2\bar{\psi}\bar{\nabla}\bar{\phi}, \tag{11}$$

$$\bar{\nabla}^2\bar{\phi} = 0, \tag{12}$$

$$\bar{\nabla}^2\bar{\psi} = \varepsilon^{-2-c}\frac{A^2}{\bar{\zeta}}\sinh(\bar{\zeta}\bar{\psi}). \tag{13}$$

These are the dimensionless equations that we will use for the process of homogenization. Here $\mathrm{Re} = \rho_0 U_{\mathrm{ref}} L_{\mathrm{mac}}/\mu_0$ and $A = L_{\mathrm{mic}}/\lambda$ where $\lambda = \sqrt{\frac{\varepsilon_{r,0}k_B T}{2z^2e^2n_o}}$ is the characteristic Debye length.

First, for the equation governing *applied electric potential*, we write the pertinent equation as

$$\begin{aligned}&\frac{D}{D\bar{x}_i}\left(\frac{D}{D\bar{x}_i}\bar{\phi}^{\varepsilon}\right)\\ &= \left(\bar{\nabla}_{x_i} + \varepsilon^{-1}\bar{\nabla}_{y_i}\right)\left(\bar{\nabla}_{x_i} + \varepsilon^{-1}\bar{\nabla}_{y_i}\right)[\varepsilon^q\bar{\phi}_0 + \varepsilon^{q+1}\bar{\phi}_1\\ &\quad + \varepsilon^{q+2}\bar{\phi}_2 + O(\varepsilon^{q+3})] = 0,\end{aligned} \tag{14}$$

which yields the leading order term as

$$\bar{\nabla}_{y_i}\bar{\nabla}_{y_i}\bar{\phi}_0 = 0. \tag{15}$$

Next, we consider the asymptotic expansion of the equation governing the *EDL potential distribution* Eq. (13).

On the left-hand side,

$$\begin{aligned}\frac{D}{D\bar{x}_i}\left(\frac{D}{D\bar{x}_i}\bar{\psi}^{\varepsilon}\right) &= \left(\bar{\nabla}_{x_i} + \varepsilon^{-1}\bar{\nabla}_{y_i}\right)\left(\bar{\nabla}_{x_i} + \varepsilon^{-1}\bar{\nabla}_{y_i}\right)[\varepsilon^e\bar{\psi}_0\\ &\quad + \varepsilon^{e+1}\bar{\psi}_1 + \varepsilon^{e+2}\bar{\psi}_2 + O(\varepsilon^{e+3})],\end{aligned} \tag{16}$$

which yields the leading order expansion term as

$$\varepsilon^{e-2} : \bar{\nabla}_{y_i}\bar{\nabla}_{y_i}\bar{\psi}_0. \tag{17}$$

Next, we take the right-hand side of the equation where we take only the first two orders in the sinh term by neglecting the higher order terms and expand it:

$$\begin{aligned}&\varepsilon^{-2-c}\frac{A^2}{\bar{\zeta}}\sinh[\bar{\zeta}(\varepsilon^e\bar{\psi}_0 + \varepsilon^{e+1}\bar{\psi}_1)]\\ &= \varepsilon^{-2-c}\frac{A^2}{\bar{\zeta}}[\sinh(\varepsilon^e\bar{\zeta}\bar{\psi}_0)\cosh(\varepsilon^{e+1}\bar{\zeta}\bar{\psi}_1)\\ &\quad + \cosh(\varepsilon^e\bar{\zeta}\bar{\psi}_0)\sinh(\varepsilon^{e+1}\bar{\zeta}\bar{\psi}_1)].\end{aligned} \tag{18}$$

Since ε is a small parameter and noting that ψ_1 will be small since it is considered to be part of perturbation of a convergent series, we can write the leading order term of the right-hand side as

$$\varepsilon^{e-2-c} : \frac{A^2}{\bar{\zeta}}\sinh(\bar{\zeta}\bar{\psi}_0). \tag{19}$$

Equating the orders of two sides, we get $c = 0$, and we get the leading order term of the potential distribution equation as

$$\bar{\nabla}_{y_i}\bar{\nabla}_{y_i}\bar{\psi}_0 = \frac{A^2}{\bar{\zeta}}\sinh(\bar{\zeta}\bar{\psi}_0). \tag{20}$$

Writing the *continuity equation* in terms of ε we get

$$\frac{D}{D\bar{x}_i}\left(\bar{v}_i^{\varepsilon}\right) = \left(\bar{\nabla}_{x_i} + \varepsilon^{-1}\bar{\nabla}_{y_i}\right)\left[\bar{v}_i^0 + \varepsilon\bar{v}_i^1 + \varepsilon^2\bar{v}_i^2 + O(\varepsilon^3)\right] = 0. \tag{21}$$

Separating different orders of ε we get

$$\varepsilon^{-1} : \bar{\nabla}_{y_i}\bar{v}_i^0 = 0, \tag{22}$$

$$\varepsilon^0 : \bar{\nabla}_{y_i}\bar{v}_i^1 + \bar{\nabla}_{x_i}\bar{v}_i^0 = 0. \tag{23}$$

Equation (22) describes the microscopic equation for the continuity, while Eq. (23) is the equation that links the microscopic and macroscopic velocity fields.

In a similar fashion, we consider the asymptotic expansion of the terms appearing in the *momentum equation* Eq. (11).

The *inertia term* yields

$$\begin{aligned}&\varepsilon^{b-a}\mathrm{Re}\left(\bar{v}_k^{\varepsilon}\frac{D}{D\bar{x}_k}\bar{v}_i^{\varepsilon}\right)\\ &= \varepsilon^{b-a}\left\{\left[\bar{v}_k^0 + \varepsilon\bar{v}_k^1 + \varepsilon^2\bar{v}_k^2 + O(\varepsilon^3)\right]\left(\bar{\nabla}_{x_k} + \varepsilon^{-1}\bar{\nabla}_{y_k}\right)\right.\\ &\quad \left.\times\left[\bar{v}_i^0 + \varepsilon\bar{v}_i^1 + \varepsilon^2\bar{v}_i^2 + O(\varepsilon^3)\right]\right\}.\end{aligned} \tag{24}$$

The leading order term is

$$\varepsilon^{b-a-1} : \mathrm{Re}\bar{v}_k^0\bar{\nabla}_{y_k}\bar{v}_i^0. \tag{25}$$

The pressure gradient term yields

$$\begin{aligned}\varepsilon^{-a}\frac{D}{D\bar{x}_i}\bar{p}^{\varepsilon} &= \varepsilon^{-a}\left(\bar{\nabla}_{x_i} + \varepsilon^{-1}\bar{\nabla}_{y_i}\right)[\varepsilon^s\bar{p}_0 + \varepsilon^{s+1}\bar{p}_1\\ &\quad + \varepsilon^{s+2}\bar{p}_2 + O(\varepsilon^{s+3})]\end{aligned} \tag{26}$$

whose leading order terms are

$$\varepsilon^{s-a-1} : \bar{\nabla}_{y_i}\bar{p}_0, \tag{27}$$

$$\varepsilon^{s-a} : \bar{\nabla}_{y_i}\bar{p}_1 + \bar{\nabla}_{x_i}\bar{p}_0. \tag{28}$$

The viscous term yields

$$\begin{aligned}\frac{D}{D\bar{x}_k}\left(\frac{D}{D\bar{x}_k}\bar{v}_i^{\varepsilon}\right) &= \left(\bar{\nabla}_{x_k} + \varepsilon^{-1}\bar{\nabla}_{y_k}\right)\left(\bar{\nabla}_{x_k} + \varepsilon^{-1}\bar{\nabla}_{y_k}\right)\left[\bar{v}_i^0 + \varepsilon\bar{v}_i^1\right.\\ &\quad \left.+ \varepsilon^2\bar{v}_i^2 + O(\varepsilon^3)\right].\end{aligned} \tag{29}$$

The leading order term is

$$\varepsilon^{-2} : \bar{\nabla}_{y_k}\left(\bar{\nabla}_{y_k}\bar{v}_i^0\right). \tag{30}$$

The electrical body force term yields

$$\varepsilon^{c-a}\frac{D}{D\bar{x}_k}\left(\frac{D}{D\bar{x}_k}\bar{\psi}^{\varepsilon}\right)\frac{D}{Dx_i}\bar{\phi}^{\varepsilon} = \varepsilon^{c-a}\left(\bar{\nabla}_{x_k}+\varepsilon^{-1}\bar{\nabla}_{y_k}\right)\left\{\left(\bar{\nabla}_{x_k}+\varepsilon^{-1}\bar{\nabla}_{y_k}\right)[\varepsilon^{e}\bar{\psi}_0+\varepsilon^{e+1}\bar{\psi}_1 + \varepsilon^{e+2}\bar{\psi}_2+O(\varepsilon^{e+3})]\right\}\left(\bar{\nabla}_{x_i}+\varepsilon^{-1}\bar{\nabla}_{y_i}\right)[\varepsilon^{q}\bar{\phi}_0+\varepsilon^{q+1}\bar{\phi}_1 + \varepsilon^{q+2}\bar{\phi}_2+O(\varepsilon^{q+3})]. \quad (31)$$

The leading order term is

$$\varepsilon^{e+q+c-a-3} : \bar{\nabla}_{y_k}\left(\bar{\nabla}_{y_k}\bar{\psi}_0\right)\bar{\nabla}_{y_i}\bar{\phi}_0. \quad (32)$$

Before collecting the terms with the same powers of ε, the values of the s, e, q, a, and b must be determined. The macroscopic pressure gradient term is of the order $s-a$, the microscopic inertia term is of the order $b-a-1$, the microscopic viscous force is of the order -2, and the electrical body force is of the order $e+q-a-3$. It is important to note that the percolation flow velocity in porous materials is normally small, and the flow Reynolds number is often less than unity. We therefore assume the flow to be a Stokes-like flow, which is valid for most cases. The order of the inertia term should thus be less than that of the viscous term, and the other three terms of the momentum equation, *viz.,* the macroscopic pressure gradient, the viscous force, and the electrical body force should balance each other (cases where the flow Reynolds number is not negligible, the inertia term could not be neglected and the up-scaled permeability tensor will have a nonlinear contribution arising due to the inertia term; see the Appendix for details). Therefore, we take $a=0$, $b=0$, $s=-2$, $e=0$, and $q=1$. With this parameter choice, we rewrite the momentum equation as

$$\varepsilon^{-3}\left(-\bar{\nabla}_{y_i}\bar{p}_0\right)+\varepsilon^{-2}\left(-\bar{\nabla}_{x_i}\bar{p}_0-\bar{\nabla}_{y_i}\bar{p}_1+\bar{\nabla}_{y_k}\bar{\nabla}_{y_k}\bar{v}_i^0 + \bar{\nabla}_{y_k}\bar{\nabla}_{y_k}\bar{\psi}_0\bar{\nabla}_{y_i}\bar{\phi}_0\right)+O(\varepsilon^{-1})=0. \quad (33)$$

The first expansion term of the momentum equation tells us that $\bar{p}_0$ depends only on the macroscopic variable $\bar{x}_i$ and not on $\bar{y}_i$, i.e.,

$$\bar{p}_0(\bar{x}_i,\bar{y}_i)=\bar{p}_0(\bar{x}_i). \quad (34)$$

The second term of the expansion governs the microscopic transport of momentum in the cell and is given by

$$-\bar{\nabla}_{x_i}\bar{p}_0-\bar{\nabla}_{y_i}\bar{p}_1+\bar{\nabla}_{y_k}\bar{\nabla}_{y_k}\bar{v}_i^0+\bar{\nabla}_{y_k}\bar{\nabla}_{y_k}\bar{\psi}_0\bar{\nabla}_{y_i}\bar{\phi}_0=0. \quad (35)$$

The boundary value problem describing the microscopic transport through the representative volume element is thus given as

$$\bar{\nabla}_{y_i}\bar{v}_i^0=0 \text{ in } Y_f, \quad (36a)$$

$$-\bar{\nabla}_{x_i}\bar{p}_0-\bar{\nabla}_{y_i}\bar{p}_1+\bar{\nabla}_{y_k}\bar{\nabla}_{y_k}\bar{v}_i^0+\bar{\nabla}_{y_k}\bar{\nabla}_{y_k}\bar{\psi}_0\bar{\nabla}_{y_i}\bar{\phi}_0=0 \text{ in } Y_f, \quad (36b)$$

$$\bar{\nabla}_{y_i}\bar{\nabla}_{y_i}\bar{\phi}_0=0 \text{ in } Y_f, \quad (36c)$$

$$\bar{\nabla}_{y_i}\bar{\nabla}_{y_i}\bar{\psi}_0=\frac{A^2}{\bar{\zeta}}\sinh[\bar{\zeta}(\bar{\psi}_0)] \text{ in } Y_f, \quad (36d)$$

$$\bar{\psi}_0=1 \text{ at } \Gamma_{fs}, \quad (36e)$$

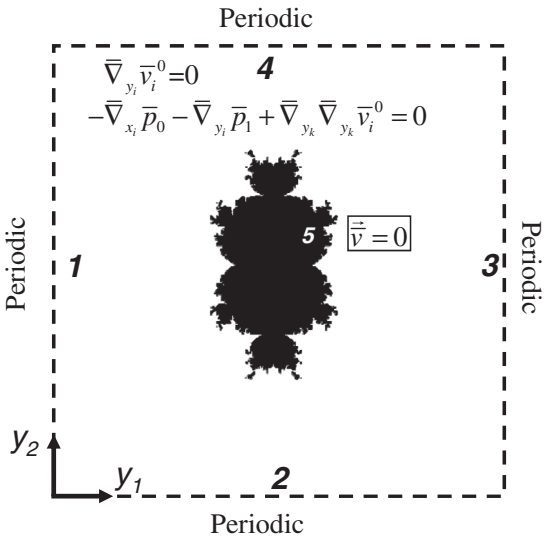

FIG. 2. Schematic of the cell problem highlighting the boundary conditions (equations written in the box) and the governing differential equations for an up-scaling Darcy-permeability tensor. Boundary pairs (1, 3) and (2, 4) are periodic in space.

$$\vec{\bar{v}}=0 \text{ at } \Gamma_{fs}, \quad (36f)$$

$$\partial_n\bar{\phi}_0=0 \text{ at } \Gamma_{fs}. \quad (36g)$$

The above set of equations is solved subjected to periodic boundary conditions to determine $\bar{v}^0$, $\bar{p}_1$, $\bar{\phi}_0$, and $\bar{\psi}_0$. Because of the linearity of the set of microscopic transport equations, the macroscopic velocity is expected to follow linear superposition of the effect due to the two flow actuating mechanisms *viz.,* the applied pressure gradient and electric field. We, therefore, consider the effects of the imposed pressure gradient and the external fields and seek the individual up-scaled permeability tensors and then superimpose the two effects for cases where the two actuating mechanisms are applied simultaneously.

Let us first consider the case where the flow across the unit cell is driven by the imposed pressure gradient. Homogenization-based up-scaling of the Darcy permeability tensor is well studied and discussed in detail elsewhere [49,50]. However, in the present article, we retrace the path for the sake of completeness. The boundary value problem describing the microscopic transport through the unit cell is given as

$$\bar{\nabla}_{y_i}\bar{v}_i^0=0 \text{ in } Y_f, \quad (37a)$$

$$-\bar{\nabla}_{x_i}\bar{p}_0-\bar{\nabla}_{y_i}\bar{p}_1+\bar{\nabla}_{y_k}\bar{\nabla}_{y_k}\bar{v}_i^0=0 \text{ in } Y_f, \quad (37b)$$

$$\bar{v}_i^0=0 \text{ at } \Gamma_{fs}, \quad (37c)$$

$$\bar{v}_i^0 \text{ is } Y\text{-periodic}. \quad (37d)$$

The above set of equations (schematically shown in Fig. 2 with appropriate governing equations and boundary conditions) is solved subjected to periodic boundary conditions to determine the unknowns $\bar{v}^0$ and $\bar{p}^1$, using a finite volume formalism in an unstructured mesh. A first order upwind scheme is used for discretizing the equations and the SIMPLE algorithm [47]

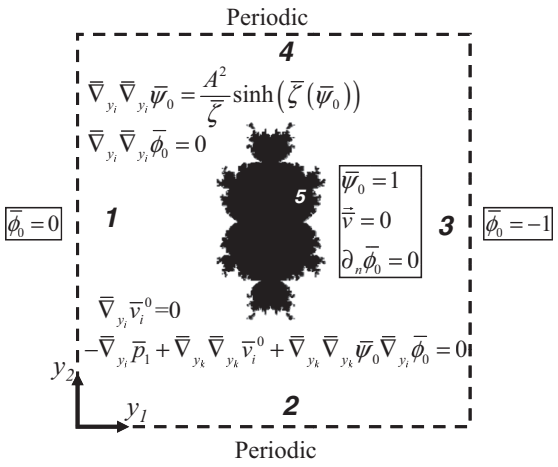

FIG. 3. Schematic of the cell problem highlighting the boundary conditions (equations written in the box) and the governing differential equations for up-scaling electro-permeability tensor. Boundary pairs (1, 3) and (2, 4) are periodic in space for the velocity, pressure, and ψ field. The figure schematically shows the boundary conditions when the applied electric field is imposed in the X_1 direction. Boundary 5 represents the boundary of the solid surface.

is used for pressure-velocity coupling on a collocated grid. The algebraic-multigrid solver [48] is used for solving the discretized equations.

The solution of the above set of equations is of the form

$$\bar{\bar{v}}_P^0(\bar{\bar{x}},\bar{\bar{y}}) = -\overleftrightarrow{k}_D(\bar{\bar{y}})\cdot\bar{\nabla}_x\bar{p}^0(\bar{\bar{x}}), \tag{38}$$

$$\bar{p}^1(\bar{\bar{x}},\bar{\bar{y}}) = -\vec{\tau}(\bar{\bar{y}})\cdot\bar{\nabla}_x\bar{p}^0(\bar{\bar{x}}) + \langle\bar{p}^1\rangle(\bar{\bar{x}}), \tag{39}$$

where $\overleftrightarrow{k}_D(y)$ gives the microscopic variation of the filtration velocity, $\vec{\tau}(y)$ gives the distribution of the microscopic pressure field in the domain, and $\langle\cdot\rangle = \frac{1}{|\Omega|}\int_\Omega\cdot\,dV$.

Integrating the ε^1 term of the continuity equation over the period, we get

$$\frac{1}{|\Omega|}\int_\Omega\bar{\nabla}_y\bar{\bar{v}}^1 dV + \frac{1}{|\Omega|}\int_\Omega\bar{\nabla}_x\bar{\bar{v}}^0 dV = 0. \tag{40}$$

Due to periodicity and the boundary conditions, we have

$$\int_\Omega\bar{\nabla}_y\bar{\bar{v}}^1\,dV = \int_{\partial\Omega}\bar{\bar{v}}^1\cdot\hat{n}\,dS = 0. \tag{41}$$

Therefore, Eq. (40) becomes

$$\frac{1}{|\Omega|}\int_\Omega\bar{\nabla}_x\bar{\bar{v}}^0 dV = \bar{\nabla}_x\cdot\left(\frac{1}{|\Omega|}\int_\Omega\bar{\bar{v}}^0 dV\right) = \bar{\nabla}_x\langle\bar{\bar{v}}^0\rangle_\Omega = 0. \tag{42}$$

We have Darcy's law given by $\langle v_P^0\rangle_\Omega = -\overleftrightarrow{K}_D\cdot\bar{\nabla}_x\bar{p}^0$ where

$$\overleftrightarrow{K}_D = \langle\overleftrightarrow{k}_D\rangle_\Omega = \frac{1}{|\Omega|}\int_\Omega\overleftrightarrow{k}_D\,dV \tag{43}$$

is the permeability tensor. The first order macroscopic behavior for the flow in the two-phase region is given by Eqs. (42) and (43) as

$$\bar{\nabla}_x(\overleftrightarrow{K}_D\cdot\bar{\nabla}_x p^0) = 0. \tag{44}$$

Thus, the components of the permeability tensor can be obtained by evaluating the $\bar{v}_1^0$ and $\bar{v}_2^0$ for the cases when the pressure gradient is applied along directions 1 and 2, respectively.

Next, we consider the case of externally applied electric field, $\bar{\bar{E}}$, on to the porous media and in this case, the externally applied pressure gradient, $\bar{\nabla}_x\bar{p}_1$ is absent. However, there will be an induced pressure gradient $\bar{\nabla}_y\bar{p}_1$ in the domain as a result of the electro-osmotic flow. The governing equations dictating the transport through the porous media are the following:

$$\bar{\nabla}_{y_i}\bar{v}_i^0 = 0 \quad \text{in} \quad Y_f, \tag{45a}$$

$$-\bar{\nabla}_{y_i}\bar{p}_1 + \bar{\nabla}_{y_k}\bar{\nabla}_{y_k}\bar{v}_i^0 + \bar{\nabla}_{y_k}\bar{\nabla}_{y_k}\bar{\psi}_0\bar{\nabla}_{y_i}\bar{\phi}_0 = 0 \quad \text{in} \quad Y_f, \tag{45b}$$

$$\bar{\nabla}_{y_i}\bar{\nabla}_{y_i}\bar{\phi}_0 = 0 \ \text{ in } \ Y_f, \tag{45c}$$

$$\bar{\nabla}_{y_i}\bar{\nabla}_{y_i}\bar{\psi}_0 = \frac{A^2}{\bar{\zeta}}\sinh[\bar{\zeta}(\bar{\psi}_0)] \ \text{ in } \ Y_f, \tag{45d}$$

$$\bar{v}_i^0 = 0 \quad \text{at} \quad \Gamma_{fs}, \tag{45e}$$

$$\bar{v}_i^0 \ \text{ is } Y\text{-periodic}, \tag{45f}$$

$$\bar{\psi}_0 = 1 \ \text{ at } \ \Gamma_{fs}, \tag{45g}$$

$$\partial_n\bar{\phi}_0 = 0 \ \text{ at } \ \Gamma_{fs}. \tag{45h}$$

The objective is to derive a homogenized parameter which would effectively represent the intricate microscopic phenomenon via a single macroscopic parameter with the obvious loss of information at the microscale. The electro-osmotic flow velocity across the porous media can be calculated by integrating the local velocity field across the unit cell. Because of the linearity, the flow velocity across the unit cell is proportional to the applied electric field $\bar{\bar{E}}$. Toward this, we analogously define the "electro-permeability" parameter which relates the macroscopic velocity to the applied potential field as

$$\bar{\bar{v}}_E^0(\bar{\bar{x}},\bar{\bar{y}}) = \overleftrightarrow{k}_E(\bar{\bar{y}})\cdot\bar{\bar{E}}(\bar{\bar{x}}), \tag{46}$$

where $\overleftrightarrow{k}_E(\bar{y})$ gives the microscopic variation of the filtration velocity because of the applied dimensionless electric field $\bar{\bar{E}} = (\bar{\nabla}\phi_0)_L$.

To determine the homogenized parameter, we once again use the higher order term of the continuity equation (42) to arrive at the first order macroscopic behavior:

$$\bar{\nabla}_x\langle\bar{\bar{v}}_E^0\rangle_\Omega = \bar{\nabla}_x\langle\overleftrightarrow{k}_E(\bar{y})\cdot\bar{\bar{E}}\rangle_\Omega = 0, \tag{47}$$

where

$$\overleftrightarrow{K}_E = \langle\overleftrightarrow{k}_E\rangle_\Omega = \frac{1}{|\Omega|}\int_\Omega\overleftrightarrow{k}_E\,dV. \tag{48}$$

is the electro-permeability tensor.

Equation (48) describes the dimensionless effective electro-permeability tensor as a function of the volume integral of velocity over the entire computational domain, thereby exhibiting a topographical sensitivity. Thus, the components of the electro-permeability tensor can be obtained by evaluating the $\bar{v}_1^0$ and $\bar{v}_2^0$ for the cases when the applied electric field is in X_1 and X_2 direction, respectively.

III. RESULTS AND DISCUSSIONS

In order to maximize the surface to volume ratio, which augments transport characteristics, natural objects form self-similar branched microstructures. Some of the examples from the living world include plants, alveoli in lungs, or the physiological passages in the circulatory system. Examples from the inanimate nature include rivers, clouds, crystal growth, and the natural porous structures. In general, fractals can be used to describe these naturally occurring structures. The porous passages encountered in natural world are often fractals in nature. Inspired by this, we consider the porous microstructures to be of fractal nature for the first part of our study, where we delineate the basic steps that need to be followed in order to calculate the permeability tensors. Next, we will proceed forward with some in-depth analysis of the electro-permeability tensor. In the first part of the study, for proof concept, we will use simulated fractal porous structures. The surface of the porous microstructure is generated using the Mandelbrot set generator [46]. The Mandelbrot set generator is created by using an iterative formula $w \to w^n + C$ for a given number of iterations where w and C are complex. We start with $w = 0$ and C is initialized to each point in the domain. Accordingly, as per the value of C, if the amplitude of w at the end of iterations escapes to infinity, we denote it by white (representing the liquid domain), or else it is denoted by black (representing the solid domain). Different Mandelbrot indices (n) lead to different microstructures with varied geometrical forms. We consider microstructures with five different values of n (3, 4, 5, 6, and 7), which represent varying levels of y_1-y_2 symmetry (morphologies shown in Fig. 7). In the next section, we consider a binary composite porous media structure, where the two components have a contrast in the ζ potential. In this part of the study, we will use random autocorrelated periodic field generator to simulate a topographically complicated porous structure. It is important to mention here that to generate the Mandelbrot sets invoked here, we have used 20 iterative cycles to generate the figures with a grid resolution of 100×100 grids.

A. Evaluation of the permeability tensors

In this section, we briefly go through the steps that need to be followed in order to evaluate the permeability tensors. In order to calculate the Darcy-permeability tensor, for pressure-driven flow, we solve the microscopic transport equation (37) through the unit cell subjected to a unit pressure gradient. A periodicity condition for the velocity and the pressure fields across the unit cell is also imposed. The velocity fields for the cases when the pressure gradient is applied along x_1 and x_2 directions are shown in Fig. 4(a) and Fig. 4(b), respectively for a particular case of $n = 4$, $f_l = 0.75$, where f_l is the liquid fraction. Once the distribution of the microscopic filtration velocity ($\vec{\bar{v}}^0$) is known, the Darcy-permeability tensor can be calculated using Eqs. (38) and (43).

In order to calculate the electro-permeability tensor, for electro-osmotic flow, we solve the microscopic transport equations (45a)–(45d) through the unit cell subjected to unit magnitude of the applied field. First, we solve the equation for the applied and the induced potential fields using Eqs. (45c)

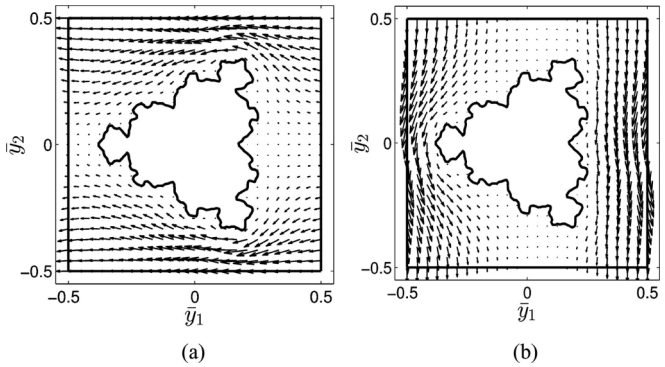

FIG. 4. Pressure-driven flow: Velocity field ($\vec{\bar{v}}^0$) for the particular case of $n = 4$, $f_l = 0.75$, for cases when the (a) applied pressure gradient is along x_1 or (b) applied pressure gradient is along x_2.

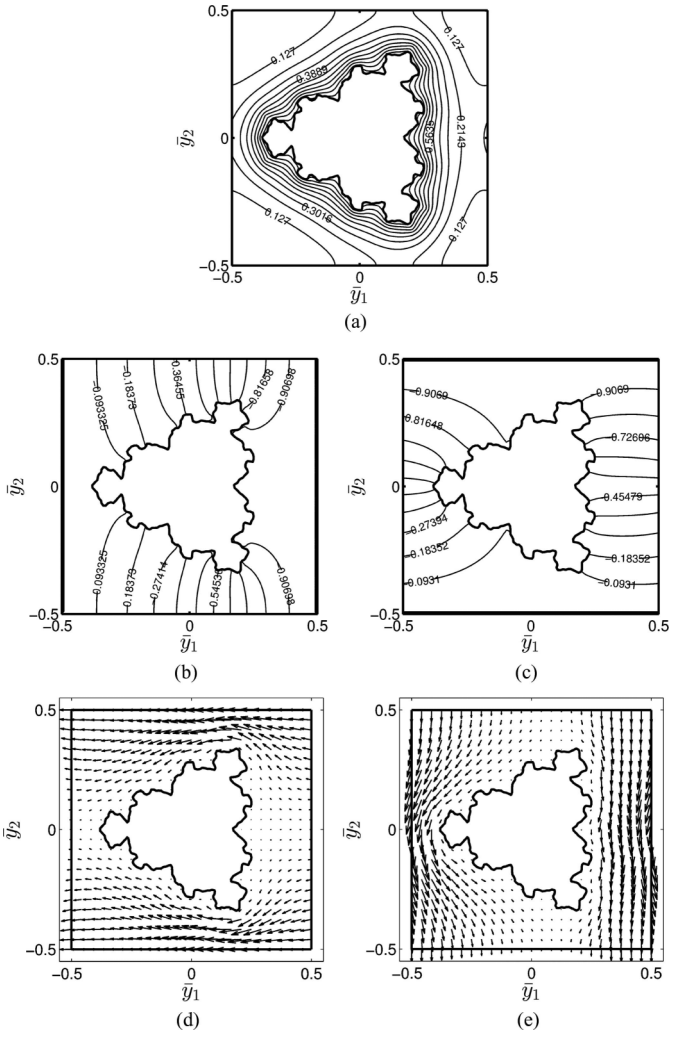

FIG. 5. Electro-osmotic flow: (a) Induced potential field ($\bar{\psi}_0$), (b) applied potential field ($\bar{\phi}_0$) when a field is applied along the x_1 direction, (c) applied potential field ($\bar{\phi}_0$) when a field is applied along the x_2 direction, (d) velocity field ($\vec{\bar{v}}_0$) when a field is applied along the x_1 direction, (e) velocity field ($\vec{\bar{v}}_0$) when a field is applied along the x_1 direction. All the cases correspond to $n = 4$ and $f_l = 0.75$.

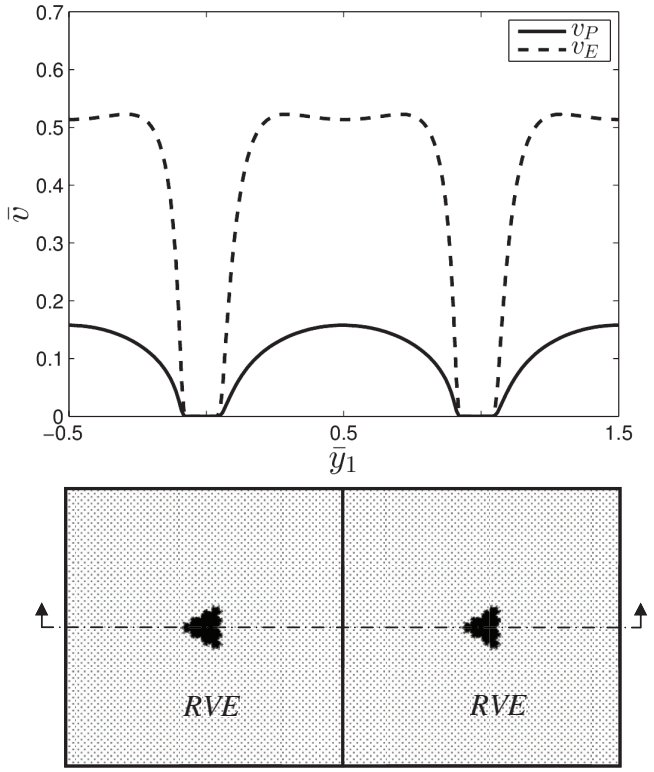

FIG. 6. Comparison of the velocity profiles at the midplane of two periodically repeated unit cells. Pressure-driven profile shows a typical parabolic nature, whereas the electro-osmotic case shows a typical plug-type profile.

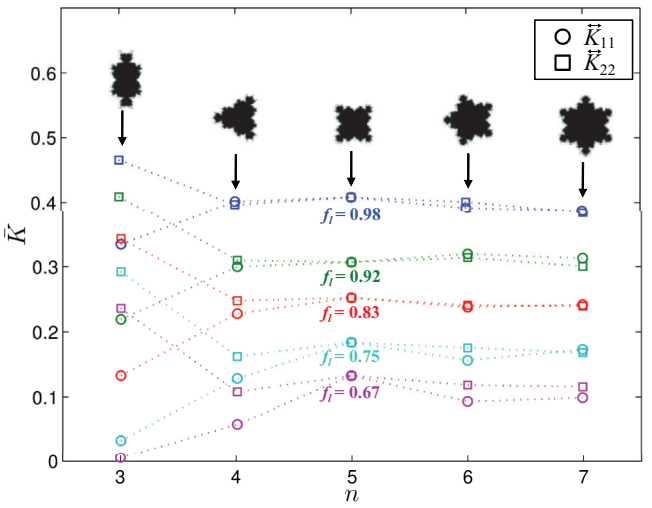

FIG. 7. (Color online) Variation of the tensor components of the electro-permeability parameter as a function of the Mandelbrot fractal index (n) for different liquid fractions. K_{11} and K_{22} represent the principal components of the permeability tensor along the coordinate directions. The curves depict a decreasing significance of the Mandelbrot index especially at a lower solid fraction. Also, the sphericity increases with increase in the Mandelbrot index.

and (45d) subjected to boundary condition given by Eqs. (45g) and (45h). We apply a field of unit magnitude by setting $\bar{\phi}_0 = 0$ and $\bar{\phi}_0 = -1$ at the left and right boundaries of the unit cell respectively. The distribution of the induced potential field ($\bar{\psi}_0$) is shown in Fig. 5(a) for a particular case of $n = 4$, $f_l = 0.75$. The applied potential field ($\bar{\phi}_0$) for cases when the field is applied along the x_1 and x_2 directions is shown in Fig. 5(b) and Fig. 5(c), respectively. Once the potential fields are known, we solve the continuity and momentum equation (45a) and (45b) subjected to boundary conditions 45(e) and 45(f). The velocity fields for the cases when the field is applied along x_1 and x_2 directions are shown in Fig. 5(a) and Fig. 5(b), respectively. The distribution of the microscopic filtration velocity ($\bar{\bar{v}}^0$) is then used to calculate the electro-permeability tensor using Eqs. (46) and (48).

It is important to note that the nature of the velocity fields for pressure-driven flow and electro-osmotic flow, shown in Figs. 4(a) and 4(b) and Figs. 5(d) and 5(e), respectively, is different as the nature of the flow-actuating mechanisms is completely different. In order to highlight this, we compare the velocity profiles at the midplanes of two periodic RVEs/REVs (shown in Fig. 6) for a lower solid fraction case ($f_l = 0.98$) where the difference between the profiles is more pronounced. For the case of pressure-driven flow, we obtain a parabolic profile, typical to pressure driven flows, and for the electro-osmotic case, we obtain a plug-type profile, which is typical to such cases.

B. The electro-permeability tensor

The Darcy-permeability tensor, arising in the case of the pressure-driven flow, is well studied in the literature [49]. In this section, we thus focus on some in-depth study of the electro-permeability tensor. Figure 7 depicts the variation of the two components of the electro-permeability tensor as a function of the Mandelbrot fractal index for the five different volume fractions ($f_l = 0.98$, 0.92, 0.83, 0.75, and 0.67). It can be seen that for higher liquid fraction values, one obtains a higher value of the permeability tensor components as compared to the ones with lower liquid fraction as the resistance to flow decreases with a decrease in the solid fraction (or equivalently with increase in liquid fraction). Moreover, the two diagonal components of the electro-permeability tensor show a large difference at low Mandelbrot index, which decreases to a large extent as the Mandelbrot index is progressively increased. This is because, as the Mandelbrot index is increased, the sphericity of the microstructure tends to increase, and with a successive increase in Mandelbrot index, n, the morphology tends toward a circle by losing the y_1-y_2 distinctness. This fact is reflected by the decrease in the difference between the diagonal components of the tensor. In the case where the solid fraction is small, we may note that the differences between the two components decreases further because the flow characteristics become insensitive to the details in the topography at low solid fractions. As the liquid fraction is increased, the values of the permeability increase in a more or less linear fashion and as the Mandelbrot index increases, all the values tend to crowd toward a limit because of the combined effect of the decreasing sensitivity of the flow structures toward details of the microstructure (with increase in liquid fraction) and increasing sphericity of the microstructures (with increase in n). In essence, this figure

captures the topographical and solid fraction sensitivity of the electro-permeability tensor.

Next, as an illustrative case study, we consider the case of a composite porous medium. We characterize the composite porous medium in terms of a partition fraction (PF), which is basically the ratio of the solid fractions of porous media having dimensionless ζ potentials of $\bar{\zeta}_1$ and $\bar{\zeta}_2$, respectively. Having established the topographic and volume fraction sensitivity of the electro-permeability tensor, we now focus our attention to establish the role of ζ potential contrast and partition fraction on the electro-permeability. In doing so, we consider a constant solid fraction, vary the PF, and take $\bar{\zeta}_1/\bar{\zeta}_2 = 10$. The periodic porous medium is generated by a random, auto-correlated periodic field generator as depicted in Fig. 8(a).

Figure 8(b) depicts the tensor components for a composite porous media. It is seen that for a randomly generated periodic porous media, the diagonal components of the electro-permeability tensor dominate, whereas the offdiagonal components (cross-components) have relatively lower values. It may be noted that when there is a ζ contrast existing between the two constituents, the permeability values are larger than the case where the entire medium has a single constituent having a fixed ζ potential at the respective shear planes. As the relative fraction of the component having a higher ζ potential increases, there is an increase in the overall permeability of all the porous structure. In Fig. 8(b) we have also plotted the Darcy-permeability tensor components in order to compare it with the electro-permeability tensor. It is important to note that the Darcy-permeability tensor components are around two orders of magnitude lower than the electro-permeability tensor components. The difference in the orders is due to the fact that the unit magnitudes of the pressure gradient and unit magnitude of the electric field give rise to a different distribution of the microscopic velocity in the cell and accordingly different effective macroscopic transport features.

This exercise is endeavored toward establishing the sensitivity of the permeability tensor to the topology, volume fraction, and partition fraction of the microstructure and contrast in ζ potential. Changes in any of these will lead to a change in the tensor components. The mathematical framework and the analysis outlined here are, however, generic and can effectively be utilized to obtain computationally efficient means of characterizing electro-osmotic transport through porous media.

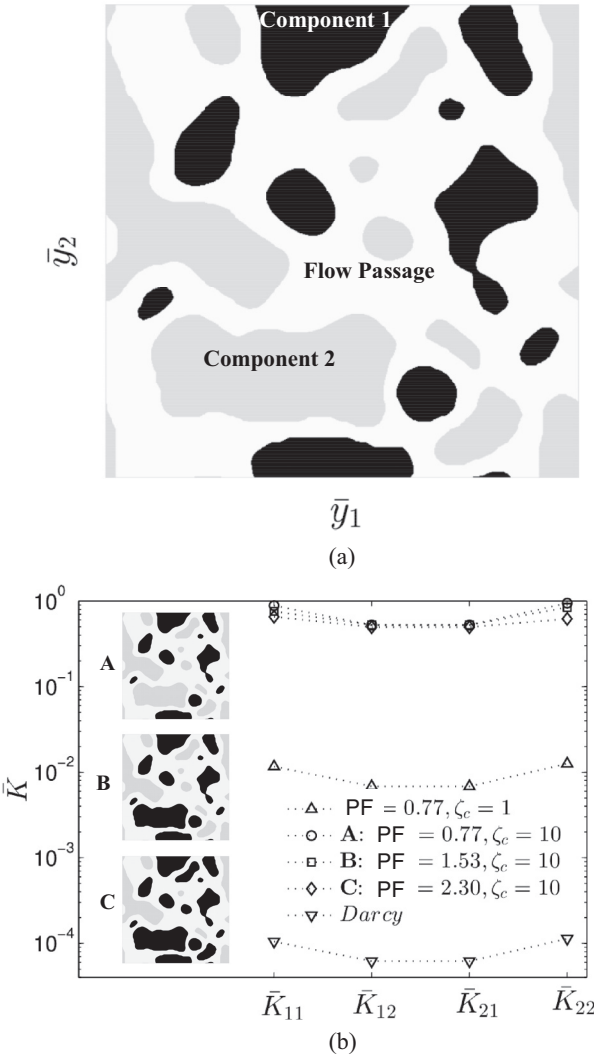

FIG. 8. (a) The randomly generated periodic morphology used in the simulation. The dark gray denotes the solid fraction having $\bar{\zeta} = -1$ and the light gray portion denotes the solid fraction having $\bar{\zeta} = -10$. The white region denotes the flow passages. (b) Variation of the electro-permeability tensor values as a function of the partition fraction and the contrast in the ζ potential. The triangle marker represents the case where the partition fraction is 0.77 and the ζ contrast ratio is 1. The circle marker represents the case where the partition fraction is 0.77 and the ζ contrast is 10. The square marker represents the case where the partition fraction is 1.53 and the ζ contrast is 10. The diamond marker represents the case where the partition fraction is 2.30 and the ζ contrast is 10. The inverted triangle marker represents the Darcy-permeability tensor components. The figure depicts that the Darcy tensor components are much lower than the electro-permeability tensor components. Also, with an increase in ζ potential contrast, the electro-permeability increases.

IV. CONCLUSIONS

Through a comprehensive analysis of electro-osmosis in porous media having complicated topology, we have derived the expression for the electro-permeability tensor, which is shown to be a function of the surface topography along with the solid fraction. We have numerically derived the various components of the electro-permeability tensor for different representative volume elements having fractal boundaries, for establishing the proof of our concept. For illustration, we have considered the case of composite porous media in which the two components have markedly different ζ potentials. We have thus established the sensitivity of the electro-permeability tensor on morphology, solid fraction, partition fraction of the phases (i.e., the ratio of solid fractions of the two phases having the two different ζ potential values), and the ζ potential contrast.

Implications of the formalism reported here are immense. This is in accordance with the fact that electro-osmotic flows through topographically complicated porous medium are of significant importance to research community. The functional dependence of the effective transport features of such flows

on the topology, solid fraction, and partition fraction of the microstructure and the contrast in ζ potential were not clearly understood and rigorously quantified until now. The developed mathematical framework, in that perspective, may be immensely helpful for devising a computationally fast and inexpensive way of accurately characterizing the electro-osmotic flows in porous media of complicated topography, without necessitating direct numerical simulation of the underlying transport phenomena over the entire flow domain.

APPENDIX: ROLE OF INERTIA: NONLINEAR CONTRIBUTION TO THE PERMEABILITY TENSOR

When the Reynolds number is small, typically much less than 1, the contribution from the inertia forces is ignored and the macroscopic pressure gradient is balanced by the leading order viscous and the electrical body forces. However, when the Reynolds number is appreciable, the inertia forces start to significantly contribute to the dynamics, and we can no longer neglect the inertia term. This is achieved through a new choice of the parameters as $a = 0$, $b = -1$, $s = -2$, $e = 0$, and $q = 1$. With this choice of parameters, we subsequently analyze the successive orders of the governing transport equations. The boundary value problem describing the microscopic transport through the representative volume element is given as

$$\bar{\nabla}_{y_i}\bar{v}_i^0(\bar{\bar{x}},\bar{\bar{y}}) = 0 \ \text{ in } \ Y_f, \tag{A1a}$$

$$\begin{aligned}&\mathrm{Re}\bar{v}_k^0(\bar{\bar{x}},\bar{\bar{y}})\bar{\nabla}_{y_k}\bar{v}_i^0(\bar{\bar{x}},\bar{\bar{y}})\\ &\quad= -\bar{\nabla}_{x_i}\bar{p}_0(\bar{\bar{x}}) - \bar{\nabla}_{y_i}\bar{p}_1(\bar{\bar{x}},\bar{\bar{y}}) + \bar{\nabla}_{y_k}\bar{\nabla}_{y_k}\bar{v}_i^0(\bar{\bar{x}},\bar{\bar{y}})\\ &\qquad+ \bar{\nabla}_{y_k}\bar{\nabla}_{y_k}\bar{\psi}_0(\bar{\bar{x}},\bar{\bar{y}})\bar{\nabla}_{y_i}\bar{\phi}_0(\bar{\bar{x}},\bar{\bar{y}}) \ \text{ in } \ Y_f,\end{aligned} \tag{A1b}$$

$$\bar{\nabla}_{y_i}\bar{\nabla}_{y_i}\bar{\phi}_0(\bar{\bar{x}},\bar{\bar{y}}) = 0 \ \text{ in } \ Y_f, \tag{A1c}$$

$$\bar{\nabla}_{y_i}\bar{\nabla}_{y_i}\bar{\psi}_0(\bar{\bar{x}},\bar{\bar{y}}) = \frac{A^2}{\bar{\zeta}}\sinh\{\bar{\zeta}[\bar{\psi}_0(\bar{\bar{x}},\bar{\bar{y}})]\} \quad \text{in} \quad Y_f, \tag{A1d}$$

$$\bar{\psi}_0(\bar{\bar{x}},\bar{\bar{y}}) = 1 \ \text{ at } \ \Gamma_{fs}, \tag{A1e}$$

$$\bar{\bar{v}}(\bar{\bar{x}},\bar{\bar{y}}) = 0 \ \text{ at } \ \Gamma_{fs}, \tag{A1f}$$

$$\partial_n\bar{\phi}_0(\bar{\bar{x}},\bar{\bar{y}}) = 0 \ \text{ at } \ \Gamma_{fs}, \tag{A1g}$$

and

$$\bar{v}_i^0(\bar{\bar{x}},\bar{\bar{y}}) \tag{A1h}$$

is Y-periodic. While calculating the permeability tensor, we drive the flow using the unit magnitude of a dimensionless pressure gradient applied across the unit cell in the case of the pressure-driven flow or unit strength of the electric field in the case of electro-osmotic flow. The momentum equation can, thus, safely be decoupled from the rest of the equations where the other equations have already been solved and the distribution of the field variables $\bar{\phi}_0$ and $\bar{\psi}_0$ is known, which can then be used to compute the momentum source while solving the continuity and momentum equations. Accordingly, in our subsequent analysis we consider the momentum equation in its generic form given as

$$\bar{\nabla}_{y_i}\bar{v}_i^0(\bar{\bar{x}},\bar{\bar{y}}) = 0 \ \text{ in } \ Y_f, \tag{A2a}$$

$$\begin{aligned}&\mathrm{Re}\bar{v}_k^0(\bar{\bar{x}},\bar{\bar{y}})\bar{\nabla}_{y_k}\bar{v}_i^0(\bar{\bar{x}},\bar{\bar{y}})\\ &\quad= -\bar{\nabla}_{y_i}\bar{p}_1(\bar{\bar{x}},\bar{\bar{y}}) + \bar{\nabla}_{y_k}\bar{\nabla}_{y_k}\bar{v}_i^0(\bar{\bar{x}},\bar{\bar{y}}) + S_{v_i}(\bar{\bar{x}},\bar{\bar{y}}) \ \text{ in } \ Y_f,\end{aligned} \tag{A2b}$$

$$\bar{\bar{v}}_i = 0 \ \text{ at } \ \Gamma_{fs}, \tag{A2c}$$

and

$$\bar{v}_i^0(\bar{\bar{x}},\bar{\bar{y}}) \tag{A2d}$$

is Y-periodic, where $S_{v_i} = -\bar{\nabla}_{x_i}\bar{p}_0(\bar{\bar{x}})$ for a pressure-driven flow and $S_{v_i} = \bar{\nabla}_{y_k}\bar{\nabla}_{y_k}\bar{\psi}_0(\bar{\bar{x}},\bar{\bar{y}})\bar{\nabla}_{y_i}\bar{\phi}_0(\bar{\bar{x}},\bar{\bar{y}})$ for an electro-osmotic flow.

In order to solve the microscopic boundary value problem on the unit cell, we split the microscopic velocity of the fluid $\bar{v}^\varepsilon$ into two components [49,50]:

$$\bar{v}^\varepsilon(\bar{\bar{x}},\bar{\bar{y}}) = \langle\bar{v}(\bar{\bar{x}})\rangle + \tilde{\bar{v}}(\bar{\bar{x}},\bar{\bar{y}}), \tag{A3}$$

where $\langle\bar{v}\rangle$ is the average microscopic velocity defined as $\langle\bar{v}(\bar{\bar{x}})\rangle = \frac{1}{|Y_f|}\int_{Y_f}\bar{v}(\bar{\bar{x}},\bar{\bar{y}})d\bar{y}$.

In the present case, we assume $\bar{v}^0(\bar{\bar{x}},\bar{\bar{y}})$ to be large, yet representing laminar flow by letting $\langle\bar{v}\rangle^0(\bar{\bar{x}})\cdot\bar{\nabla}_{y_k}\bar{v}_i^0(\bar{\bar{x}},\bar{\bar{y}})$ be possibly large with respect to $\tilde{\bar{v}}^0(\bar{\bar{x}},\bar{\bar{y}})\cdot\bar{\nabla}_{y_k}\bar{v}_i^0(\bar{\bar{x}},\bar{\bar{y}})$.

Therefore the inertial nonlinear term is linearized as follows:

$$\mathrm{Re}\bar{v}_k^0(\bar{\bar{x}},\bar{\bar{y}})\cdot\bar{\nabla}_{y_k}\bar{v}_i^0(\bar{\bar{x}},\bar{\bar{y}}) \cong \mathrm{Re}\langle\bar{v}_k^0(\bar{\bar{x}})\rangle\cdot\bar{\nabla}_{y_k}\bar{v}_i^0(\bar{\bar{x}},\bar{\bar{y}}). \tag{A4}$$

Therefore Eq. (A2) along with Eq. (A4) gives the boundary value problem as

$$\bar{\nabla}_{y_i}\bar{v}_i^0(\bar{\bar{x}},\bar{\bar{y}}) = 0 \ \text{ in } \ Y_f, \tag{A5a}$$

$$\begin{aligned}\mathrm{Re}\langle\bar{v}_k^0(\bar{\bar{x}})\rangle\bar{\nabla}_{y_k}\bar{v}_i^0(\bar{\bar{x}},\bar{\bar{y}}) &= -\bar{\nabla}_{y_i}\bar{p}_1(\bar{\bar{x}},\bar{\bar{y}}) + \bar{\nabla}_{y_k}\bar{\nabla}_{y_k}\bar{v}_i^0(\bar{\bar{x}},\bar{\bar{y}})\\ &\quad+ S_{v_i}(\bar{\bar{x}},\bar{\bar{y}}) \ \text{ in } \ Y_f,\end{aligned} \tag{A5b}$$

$$\bar{v}_i^0(\bar{\bar{x}},\bar{\bar{y}}) = 0 \ \text{ in } \ Y_f, \tag{A5c}$$

and

$$\bar{v}_i^0(\bar{\bar{x}},\bar{\bar{y}}) \tag{A5d}$$

is Y-periodic. In order to keep track of the linear component of the permeability tensor, the first term of the velocity expansion and the second term of the pressure one are split as [49,50]

$$\bar{v}^0(\bar{\bar{x}},\bar{\bar{y}}) = \bar{v}^\alpha(\bar{\bar{x}},\bar{\bar{y}}) + \bar{v}^\beta(\bar{\bar{x}},\bar{\bar{y}},\langle\bar{v}^0\rangle), \tag{A6}$$

and

$$\bar{\nabla}_y\bar{p}^1(\bar{\bar{x}},\bar{\bar{y}}) = \bar{\nabla}_y\bar{p}_\alpha^1(\bar{\bar{x}},\bar{\bar{y}}) + \bar{\nabla}_y\bar{p}_\beta^1(\bar{\bar{x}},\bar{\bar{y}}). \tag{A7}$$

Introducing Eq. (A6) and Eq. (A7) in the momentum equation, we obtain the governing transport equations for the velocity fields $\bar{v}^\alpha(\bar{\bar{x}},\bar{\bar{y}})$ and $\bar{v}^\beta(\bar{\bar{x}},\bar{\bar{y}},\langle\bar{v}^0\rangle)$ respectively as

$$0 = -\bar{\nabla}_{y_i}\bar{p}_\alpha^1(\bar{\bar{x}},\bar{\bar{y}}) + \bar{\nabla}_{y_k}\bar{\nabla}_{y_k}\bar{v}_i^\alpha(\bar{\bar{x}},\bar{\bar{y}}) + S_{v_i}(\bar{\bar{x}},\bar{\bar{y}}), \tag{A8}$$

$$\begin{aligned}&\mathrm{Re}\langle\bar{v}_k^0\rangle(\bar{x})\bar{\nabla}_{y_k}\bar{v}_i^\beta(\bar{\bar{x}},\bar{\bar{y}},\langle\bar{v}^0\rangle)\\ &\quad= -\bar{\nabla}_{y_i}\bar{p}_\beta^1(\bar{x},\bar{y}) + \bar{\nabla}_{y_k}\bar{\nabla}_{y_k}\bar{v}_i^\beta(\bar{\bar{x}},\bar{\bar{y}},\langle\bar{v}^0\rangle)\\ &\qquad- \mathrm{Re}\langle\bar{v}_k^0(\bar{\bar{x}})\rangle\bar{\nabla}_{y_k}\bar{v}_i^\alpha(\bar{\bar{x}},\bar{\bar{y}}).\end{aligned} \tag{A9}$$

The solution of Eq. (A8) is of the form

$$\bar{v}_i^{\alpha}(\bar{\bar{x}},\bar{\bar{y}}) = k_{ij}(\bar{\bar{y}})Q_j(\bar{\bar{x}}), \tag{A10}$$

where $Q_j = -\bar{\nabla}_{x_i}\bar{p}_0$ for pressure-driven flow and $Q_j = E_j$ for electro-osmotic flow.

Therefore Eq. (A6) must satisfy

$$\begin{aligned}\mathrm{Re}\langle\bar{v}_k^0(\bar{\bar{x}})\rangle\bar{\nabla}_{y_k}\bar{v}_i^{\beta}(\bar{\bar{x}},\bar{\bar{y}},\langle\bar{v}^0\rangle) &= -\bar{\nabla}_{y_i}\bar{p}_{\beta}^1(\bar{\bar{x}},\bar{\bar{y}}) + \bar{\nabla}_{y_k}\bar{\nabla}_{y_k}\bar{v}_i^{\beta}(\bar{\bar{x}},\bar{\bar{y}},\langle\bar{v}^0\rangle) \\ &\quad - \mathrm{Re}\langle\bar{v}_k^0\rangle(\bar{\bar{x}})Q_j(\bar{\bar{x}})\bar{\nabla}_{y_k}k_{ij}(\bar{\bar{y}}).\end{aligned} \tag{A11}$$

Per analogy to solution (A10), there exists a solution for the microscopic periodic field $\bar{v}^{\beta}(\bar{\bar{x}},\bar{\bar{y}},\langle\bar{v}^0\rangle)$ which satisfies

$$\bar{v}_i^{\beta}(\bar{\bar{x}},\bar{\bar{y}},\langle\bar{v}^0\rangle) = h_{ij}(\bar{\bar{y}},\langle\bar{v}^0\rangle)Q_j(\bar{\bar{x}}). \tag{A12}$$

Integrating the ε^0 term of the incompressible continuity equation over the period, we get

$$\begin{aligned}&\frac{1}{|\Omega|}\int_{\Omega}\bar{\nabla}_y\vec{v}^1\,dV + \frac{1}{|\Omega|}\int_{\Omega}\bar{\nabla}_x\vec{v}^0\,dV \\ &\quad = \frac{1}{|\Omega|}\int_{\Omega}\bar{\nabla}_y\vec{v}^1\,dV + \frac{1}{|\Omega|}\int_{\Omega}\bar{\nabla}_x(\vec{v}^{\alpha}+\vec{v}^{\beta})\,dV = 0.\end{aligned} \tag{A13}$$

Due to periodicity and the boundary conditions, we get

$$\int_{\Omega}\bar{\nabla}_y\vec{v}^1\,dV = \int_{\partial\Omega}\vec{v}^1\cdot\hat{n}\,dS = 0. \tag{A14}$$

Therefore, Eq. (A13) becomes

$$\begin{aligned}\frac{1}{|\Omega|}\int_{\Omega}\bar{\nabla}_x(\vec{v}^{\alpha}+\vec{v}^{\beta})\,dV &= \bar{\nabla}_x\cdot\frac{1}{|\Omega|}\left[\int_{\Omega}\vec{v}^{\alpha}dV + \int_{\Omega}\vec{v}^{\beta}\,dV\right] \\ &= \bar{\nabla}_x[\langle\vec{v}^{\alpha}\rangle_{\Omega} + \langle\vec{v}^{\beta}\rangle_{\Omega}] = 0,\end{aligned} \tag{A15}$$

where $\langle\cdot\rangle_{\Omega} = \frac{1}{|\Omega|}\int_{\Omega}\cdot\,dV$.

From Eqs. (A7), (A9), and (A12), we get the first order macroscopic behavior as

$$\langle v^0\rangle_{\Omega} = -\overleftrightarrow{K}\bar{\nabla}_x p^0, \tag{A16}$$

where $\overleftrightarrow{K} = \langle\overleftrightarrow{k}\rangle_{\Omega} + \langle\overleftrightarrow{h}\rangle_{\Omega}(\langle\vec{v}^0\rangle)$ is the up-scaled permeability tensor where the second term is the correction arising due to the incorporation of the nonlinear contribution due to the presence of the inertial effects. The up-scaled permeability tensor is a function of the morphology, liquid fraction, and mean macroscopic velocity in the computational cell, which in turn is a function of the flow Reynolds number and vanishes for low Reynolds number flows.

[1] M. Eikerling, A. A. Kornyshev, A. M. Kuznetsov, J. Ulstrup, and S. Walbran, J. Phys. Chem. B **105**, 3646 (2001).
[2] F. H. J. van der Heyden, D. J. Bonthuis, D. Stein, C. Meyer, and C. Dekker, Nano Lett. **7**, 1022 (2007).
[3] Y. Ren and D. Stein, Nanotechnology **19**, 195707 (2008).
[4] N. S. K. Gunda, H. Choi, A. Berson, B. Kenney, K. Karan, J. G. Pharaoh, and S. K. Mitra, J. Power Sources **196**, 3592 (2011).
[5] A. W. Martinez, S. T. Phillips, and G. M. Whitesides, Anal. Chem. **82**, 3 (2010).
[6] P. Mandal, R. Dey, and S. Chakraborty, Lab on a Chip **12**, 4026 (2012).
[7] N. S. K. Gunda, B. Bera, N. K. Karadimitriou, S. K. Mitra, and S. M. Hassanizadeh, Lab on a Chip **11**, 3785 (2011).
[8] L. G. Leal, *Advanced Transport Phenomena: Fluid Mechanics and Convective Transport Processes* (Cambridge University Press, New York, 1989).
[9] S. Ghosal, Annu. Rev. Fluid Mech. **38**, 309 (2006).
[10] R. F. Probstein, *Physicochemical Hydrodynamics: An Introduction* (John Wiley and Sons, New York, 1994), p. 400.
[11] A. S. Rathore and C. Horváth, J. Chromatogr. A **781**, 185 (1997).
[12] H. Ohshima, J. Colloid Interface Sci. **210**, 397 (1999).
[13] S. Levine and G. H. Neale, J. Colloid Interface Sci. **47**, 520 (1974).
[14] S. Levine, J. R. Marriott, G. H. Neale, and N. Epstein, J. Colloid Interface Sci. **52**, 136 (1975).
[15] F. C. Leinweber and U. Tallarek, J. Phys. Chem. B **109**, 21481 (2005).
[16] D. Coelho, M. Shapiro, and J. Thovert, J. Colloid Interface Sci. **190**, 169 (1996).
[17] S. Das, S. Chakraborty, and S. K. Mitra, Phys. Rev. E **85**, 051508 (2012).
[18] A. Bandopadhyay and S. Chakraborty, Langmuir **28**, 17552 (2012).
[19] S. Chakraborty and S. Das, Phys. Rev. E **77**, 037303 (2008).
[20] S. Das, R. Misra, T. Thundat, S. Chakraborty, and S. Mitra, Energy Fuels **26**, 5851 (2012)
[21] A. Bandopadhyay and S. Chakraborty, Phys. Rev. E **85**, 056302 (2012)
[22] S. Chakraborty, J. Phys. D **39**, 5356 (2006)
[23] J. H. Masliyah and S. Bhattacharjee, *Electrokinetic and Colloid Transport Phenomena* (John Wiley & Sons, Hoboken, NJ, 2006).
[24] A. A. Saha, S. K. Mitra, and X. Li, J. Power Sources **164**, 154 (2007).
[25] A. S. Rawool and S. K. Mitra, Microfluidics Nanofluidics **2**, 261 (2006).
[26] A. Ogawa, J. Rheol. **41**, 769 (1997).
[27] C. F. Fryling, J. Colloid Sci. **18**, 713 (1963).
[28] D. E. Elrick, D. E. Smiles, N. Baumgartner, and P. H. Groenevelt, Soil Sci. Soc. Am. J. **40**, 490 (1976).
[29] R. Hunter, *Zeta Potential in Colloid Science: Principles and Applications* (Academic Press, London, 1981).
[30] A. Dasgupta and R. K. Agarwal, J. Compos. Mater. **26**, 2736 (1992).
[31] A. J. Majda and P. E. Souganidis, Nonlinearity **7**, 1 (1994).
[32] G. Laschet, S. Rex, D. Bohn, and N. Moritz, Numer. Heat Transfer, Part A **42**, 91 (2002).
[33] G. Laschet, Comput. Methods Appl. Mech. Eng. **191**, 4535 (2002).
[34] W. Zijl and A. Trykozko, Comput. Geosci. **6**, 49 (2002).
[35] D. DasGupta, S. Basu, and S. Chakraborty, Phys. Lett. A **348**, 386 (2006).

[36] Y. Amirat and V. Shelukhin, J. Math. Anal. Appl. **342**, 1227 (2008).
[37] M. W. Kozak and E. J. Davis, J. Colloid Interface Sci. **127**, 497 (1989).
[38] Y. Kang, C. Yang, and X. Huang, Int. J. Eng. Sci. **42**, 2011 (2004).
[39] I. Glasgow, J. Batton, and N. Aubry, Lab on a Chip **4**, 558 (2004).
[40] J.-L. Auriault, C. Boutin, and C. Geindreau, *Homogenization of Coupled Phenomena in Heterogenous Media* (Wiley, Hoboken NJ, 2009).
[41] P. W. Chung, K. K. Tamma, and R. R. Namburu, Composites A Appl. Sci. Manuf. **32**, 1291 (2001).
[42] G. Allaire, A. Mikelić, and A. Piatnitski, J. Math. Phys. **51**, 123103 (2010).
[43] A. Bensoussan, J.-L. Lions, and G. Papanicolaou, *Asymptotic Analysis for Periodic Structures* (Elsevier, New York, 1978).
[44] E. Sanchez-Palencia and F. Verhulst, *Asymptotic Analysis II—Surveys and New Trends* (Springer, Berlin, 1983).
[45] H. Bruus, *Theoretical Microfluidics* (Oxford University Press, Oxford, 2007).
[46] B. Mandelbrot, Science **156**, 636 (1967).
[47] S. Patankar, *Numerical Heat Transfer and Fluid Flow* (Taylor and Francis, New Delhi, 1980).
[48] U. Trottenberg, C. W. Oosterlee, and A. Schüller, *Multigrid* (Academic Press, London, 2001).
[49] G. Laschet, J. Comput. Appl. Math. **168**, 277 (2004).
[50] T. Giorgi, Transp. Porous Media **29**, 191 (1997).